



# The JCMT Transient Survey: Single-epoch Transients and Variability of Faint Sources

Doug Johnstone<sup>1,2</sup>, Bhavana Lalchand<sup>3</sup>, Steve Mairs<sup>4,5</sup>, Hsien Shang<sup>6</sup>, Wen Ping Chen<sup>3,7</sup>, Geoffrey C. Bower<sup>8</sup>, Gregory J. Herczeg<sup>9,10</sup>, Jeong-Eun Lee<sup>11</sup>, Jan Forbrich<sup>12</sup>, Bo-Yan Chen<sup>8,13</sup>, Carlos Contreras Peña<sup>11,14</sup>, Yong-Hee Lee<sup>11</sup>, Wooseok Park<sup>11</sup>, Colton Broughton<sup>2</sup>, and Spencer Plovie<sup>2</sup>

The JCMT Transient Team

<sup>1</sup> NRC Herzberg Astronomy and Astrophysics, 5071 West Saanich Rd, Victoria, BC, V9E 2E7, Canada; [Doug.Johnstone@nrc-cnrc.gc.ca](mailto:Doug.Johnstone@nrc-cnrc.gc.ca)

<sup>2</sup> Department of Physics and Astronomy, University of Victoria, Victoria, BC, V8P 5C2, Canada

<sup>3</sup> Institute of Astronomy, National Central University, 300 Zhongda Road, Zhongli, Taoyuan 32001, Taiwan, R.O.C.

<sup>4</sup> SOFIA Science Center, Universities Space Research Association, NASA Ames Research Center, Moffett Field, CA 94035, USA

<sup>5</sup> East Asian Observatory, 600 N. A'ohoku Place, Hilo, HI 96720, USA

<sup>6</sup> Institute of Astronomy and Astrophysics, Academia Sinica, Taipei 10617, Taiwan, R.O.C.

<sup>7</sup> Department of Physics, National Central University, 300 Zhongda Road, Zhongli, Taoyuan 32001, Taiwan, R.O.C.

<sup>8</sup> Institute of Astronomy and Astrophysics, Academia Sinica, 645 N. A'ohoku Place, Hilo, HI 96720, USA

<sup>9</sup> Kavli Institute for Astronomy & Astrophysics, Peking University, Yiheyuan Lu 5, Haidian Qu, 100871 Beijing, People's Republic of China

<sup>10</sup> Department of Astronomy, Peking University, Yiheyuan 5, Haidian Qu, 100871 Beijing, People's Republic of China

<sup>11</sup> School of Space Research, Kyung Hee University, 1732, Deogyong-daero, Giheung-gu, Yongin-si, Gyeonggi-do 17104, Republic of Korea

<sup>12</sup> Centre for Astrophysics Research, University of Hertfordshire, College Lane, Hatfield, AL10 9 AB, UK

<sup>13</sup> Institute of Astronomy, National Tsing Hua University, Taiwan

<sup>14</sup> Department of Physics and Astronomy, Seoul National University, 1 Gwanak-ro, Gwanak-gu, Seoul 08826, Republic of Korea

Received 2022 May 21; revised 2022 August 12; accepted 2022 August 15; published 2022 September 15

## Abstract

Short-duration flares at millimeter wavelengths provide unique insights into the strongest magnetic reconnection events in stellar coronae and combine with longer-term variability to introduce complications to next-generation cosmology surveys. We analyze 5.5 yr of JCMT Transient Survey 850  $\mu\text{m}$  submillimeter monitoring observations toward eight Gould Belt star-forming regions to search for evidence of transient events or long-duration variability from faint sources. The eight regions (30' diameter fields), including  $\sim 1200$  infrared-selected YSOs, have been observed on average 47 times with integrations of approximately half an hour, or one day total, spread over 5.5 yr. Within this large data set, only two robust faint source detections are recovered: JW 566 in OMC 2/3 and MGM12 2864 in NGC 2023. JW 566, a Class II T Tauri binary system previously identified as an extraordinary submillimeter flare, remains unique, the only clear single-epoch transient detection in this sample with a flare eight times bright than our  $\sim 4.5\sigma$  detection threshold of  $55 \text{ mJy beam}^{-1}$ . The lack of additional recovered flares intermediate between JW 566 and our detection limit is puzzling if smaller events are more common than larger events. In contrast, the other submillimeter variable identified in our analysis, Source 2864, is highly variable on all observed timescales. Although Source 2864 is occasionally classified as a YSO, the source is most likely a blazar. The degree of variability across the electromagnetic spectrum may be used to aid source classification.

*Unified Astronomy Thesaurus concepts:* [Stellar flares \(1603\)](#); [Variable stars \(1761\)](#); [Submillimeter astronomy \(1647\)](#); [Surveys \(1671\)](#); [Young stellar objects \(1834\)](#)

## 1. Introduction

Young stellar objects (YSOs) are known for their variability due to both accretion phenomena and magnetic activity. Young low-mass pre-main-sequence stars are fully convective and therefore develop magnetospheres from stellar dynamos. High-energy events driven by the magnetosphere's magnetic field interacting with itself or its surroundings are expected to occur, producing powerful stellar flares. Monitoring the timescales and amplitude changes of their emission over time provides a useful probe of these physical processes.

Coronal flares are driven by magnetic reconnection of large loops of the field that protrude from the stellar surface. The magnetic reconnection converts magnetic energy into gas kinetic energy and bulk plasma motions. Most of the energy released is thermalized and radiated away as thermal emission, which can be measured using the soft X-ray emission from the

corona or ultraviolet line emission from the chromosphere (Benz & Güdel 2010). A fraction of the released energy is emitted at radio frequencies as gyrosynchrotron radiation (Waterfall et al. 2019), manifesting as radio flares. An empirical scaling relation,  $L_X/L_R \sim 10^{15 \pm 1} \text{ Hz}$  links the two across several orders of magnitude, although the X-rays saturate at  $\log L_X/L_{\text{bol}} \sim -3$  (Güdel & Benz 1993).

Stellar flares are typically explained as magnetic reconnection in the stellar magnetosphere. However, for young stars the largest events, such as those equivalent to coronal mass ejections, may arise from enormous loops. These loops could potentially couple to the surrounding accretion disk, if present, and enhance the magnitude of the flare (Forbrich et al. 2016, 2017). Compared with main-sequence stars, flares have an elevated importance for T Tauri stars, with X-ray flare luminosities typically ranging from  $L_X \sim 10^{28-31} \text{ erg s}^{-1}$ , comparable to the solar maximum  $L_X \sim 10^{27} \text{ erg s}^{-1}$  (Feigelson & Montmerle 1999). More recently, Getman & Feigelson (2021) identified a sample of 1000 superflares with  $L_X \sim 10^{30.5-34} \text{ erg s}^{-1}$  from YSOs, detected on both disk-bearing and diskless systems and across a wide range of

evolutionary stages, including protostars. Since many of these large flares are detected on diskless stars, the emission volume of the magnetic loops either does not require an anchor or may be amplified by anchoring the field to a nearby magnetized stellar or substellar companion (Lin et al. 2022).

Previous observations of radio flares from YSOs have been reported at millimeter (Bower et al. 2003; Furuya et al. 2003; Massi et al. 2006; Salter et al. 2008) and centimeter wavelengths (Forbrich et al. 2008, 2017). The brightest of these flares reached  $L_R \sim 10^{19} \text{ erg s}^{-1} \text{ Hz}^{-1}$  (Bower et al. 2003), many orders of magnitude higher than the M-type star radio flaring events monitored in the millimeter by MacGregor et al. (2018, 2020), and comparable to the highest superflare X-ray luminosities, assuming the empirical scaling relation. With the advent of all-sky monitoring campaigns at millimeter wavelengths by the Atacama Cosmology Telescope (ACT) and the South Pole Telescope (SPT), powerful radio flares are beginning to be detected, with  $L_R > 10^{15.5} \text{ erg s}^{-1} \text{ Hz}^{-1}$  and reaching  $L_R \sim 10^{19} \text{ erg s}^{-1} \text{ Hz}^{-1}$  (Guns et al. 2021; Naess et al. 2021). Initial analyses suggest that these flares are associated with relatively young stars (Naess et al. 2021); however, proper statistical analysis awaits significantly larger samples, such as those planned by the CCAT Observatory (CCAT-Prime collaboration et al. 2021) and CMB-S4 (Abazajian et al. 2019).

These strong flares are important not only as a diagnostic of the magnetic and dynamo processes but also for the energetic X-ray emission and MeV particles that interact with the surrounding disk. Combined, these processes lead to chemical reactions ionizing the disk, with diagnostics that include emission in Ne II (e.g., Glassgold et al. 2007; Güdel et al. 2010) and  $\text{H}^{13}\text{CO}^+$  (Cleeves et al. 2017). Finally, interactions between the MeV particles and dust grains in the disk can induce nuclear reactions, leading to short-lived radionuclides (Lee et al. 1998; Sossi et al. 2017) and heating events (see discussion by Shu et al. 1997).

The most powerful YSO radio flare observed to date,  $L_R = 8 \times 10^{19} \text{ erg s}^{-1} \text{ Hz}^{-1}$ , was detected from the Class II T Tauri binary JW 566 in Orion OMC 2/3 in the submillimeter at 450 and 850  $\mu\text{m}$  with the James Clerk Maxwell Telescope (JCMT) by Mairs et al. (2019). Converted to X-ray luminosity using the Güdel & Benz (1993) relation, that event produced  $\sim 10^{35} \text{ erg s}^{-1}$ , though it is likely that the correlation saturates at such high values. This scaled luminosity would be an order of magnitude stronger than the X-ray superflares observed by Getman & Feigelson (2021), five orders of magnitude greater than the typical T Tauri star flare, and an impressive ten orders of magnitude brighter than most solar flares. The Mairs et al. (2019) discovery, found via a preliminary search through the JCMT Transient Survey data set, recovered this single flare detected on 2016 November 26, with a decay of 50% during the 30 minute integration. The submillimeter source associated with JW 566 was not detected at any other epochs. The spectral index between the two submillimeter wavelengths,  $\alpha = 0.11$ , is broadly consistent with nonthermal emission. Together, the short submillimeter duration and low spectral index support the flare interpretation, with the brightening event likely due to magnetic reconnection energizing charged particles to emit gyrosynchrotron/synchrotron radiation. Along with the JW 566 burst having the largest radio luminosity, it is also unique by being observed at the highest frequency, 650 GHz (450  $\mu\text{m}$ ), of any YSO radio flare to date.

In this paper, we analyze 5.5 yr of JCMT Transient Survey submillimeter monitoring observations toward eight Gould Belt star-forming regions to search for evidence of variability from faint sources, primarily Class II YSOs. In Section 2, we describe the JCMT Survey, the standard data reduction procedure, and the additional processing techniques required by this paper. We present the results of our variability investigation in Section 3 and discuss the implications of our results in Section 4. The paper is summarized in Section 5.

## 2. Observations

### 2.1. JCMT Transient Survey

The JCMT Transient Survey has been monitoring eight active Gould Belt star-forming regions within 500 pc of the Sun (Herczeg et al. 2017; Mairs et al. 2017b) since 2015 December. In this paper we present an analysis of observations taken over 5.5 yr, through 2021 June. The survey is the first dedicated long-term monitoring program of YSOs at submillimeter wavelengths. Each region is observed with at least a monthly cadence,<sup>15</sup> when available. Almost 300 bright ( $>140 \text{ mJy bm}^{-1}$ ) submillimeter peaks across all regions have been investigated for variability (Mairs et al. 2017a; Johnstone et al. 2018; Lee et al. 2021b), with greater than 20% of the 83 monitored protostars showing robust evidence for long-term brightening or dimming associated with accretion processes within the disk. None of the bright protostars show evidence of single-epoch enhanced variability, and none of the submillimeter bright starless cores are found to be variable with either short or long timescales (Lee et al. 2021b).

The eight monitored star-forming regions, namely IC 348, NGC 1333, OMC 2/3, NGC 2024, NGC 2068, Ophiuchus, Serpens Main, and Serpens South (see Table 1), were selected to maximize the number of deeply embedded, Class 0/I sources. JCMT Gould Belt Survey (Ward-Thompson et al. 2007) 850  $\mu\text{m}$  coadded images were used to locate bright submillimeter peaks and collated against Spitzer YSO survey catalogs at mid- through far-IR (Megeath et al. 2012; Dunham et al. 2015). Along with the hundred odd protostars within these regions, more than 1500 known Class II YSOs (and many more Class III YSOs) are monitored by the survey (Herczeg et al. 2017), although almost all the Class II systems are too faint in the submillimeter to be detected in a single epoch. The monthly monitoring cadence was chosen based on an estimate of the thermal equilibration time for dust in a protostellar envelope coupled with the light propagation time through the envelope (Johnstone et al. 2013).

### 2.2. Map Reconstruction

SCUBA-2 is a 10,000 pixel detector, simultaneously observing a 45 arcmin<sup>2</sup> footprint at 450 and 850  $\mu\text{m}$  (Holland et al. 2013). We obtain images of 30' circular fields using the PONG1800 mode, which moves SCUBA-2 in a rotating ‘‘pong’’ pattern to obtain circular maps with consistent noise properties. Each total integration is  $\sim 20\text{--}40$  minutes, set based on the precipitable water vapor to reach a noise level of

<sup>15</sup> Occasionally, regions are monitored with a higher cadence. For example, Serpens Main, which hosts the 18 month quasiperiodic submillimeter source EC 53 (Yoo et al. 2017; Lee et al. 2020), also known as V371 Ser, is typically monitored with a 2 week cadence.

**Table 1**  
Summary of JCMT Transient Survey Regions at 850  $\mu\text{m}$

Region	R.A.	Decl.	Epochs	First	Latest	Epoch Uncertainty (mJy beam $^{-1}$ )	Mean Brightness Uncertainty (mJy beam $^{-1}$ )
	(J2000)	(J2000)		(Epoch)	(Epoch)		
IC 348	03:44:18	+31:16:52	44	22/12/2015	03/03/2021	11–16	2.0
NGC 1333	03:28:54	+31:16:52	45	22/12/2015	03/03/2021	11–13	1.8
NGC 2024	05:41:41	−01:53:51	43	26/12/2015	06/04/2021	11–12	1.9
NGC 2068	05:46:13	−00:06:05	52	26/12/2015	17/04/2021	11–14	1.6
OMC 2/3	05:35:33	−05:00:32	42	26/12/2015	06/04/2021	11–13	1.8
Ophiuchus	16:27:05	−24:32:37	34	15/01/2016	15/05/2021	11–14	2.7
Serpens Main	18:29:49	+01:15:20	67	02/02/2016	09/06/2021	11–12	1.1
Serpens South	18:30:02	−02:02:48	52	02/02/2016	02/06/2021	11–13	1.5

$\sim 12$  mJy beam $^{-1}$  at 850  $\mu\text{m}$ . The eight star-forming regions in our sample have now been observed at 850  $\mu\text{m}$  for almost one full day (see Table 1).

The raw instrumental observations at 850  $\mu\text{m}$  are affected by the “scan-synchronous” low-frequency correlation with the telescope motion (common mode) and by a combination of elevation-induced changes in sky brightness and magnetic field pickup across the detectors (see Chapin et al. 2013, for details). In addition, there is attenuation due to the atmospheric opacity, flat-field corrections, sky noise, cosmic rays, and other contaminants that are considered and removed by the map-maker. The MAKEMAP algorithm, explained in detail by Chapin et al. (2013) and provided as a part of the STARLINK software (Currie et al. 2014), is employed to produce astronomical maps from the raw data. At 850  $\mu\text{m}$ , a 3'' pixel scale is chosen in order to subsample the  $\sim 14''$  beam. In the preprocessing stage of the data reduction process, flat-field correction, time series downsampling, step correction, and despiking of the inputs are applied. This is followed by an iterative process, where common-mode removal, extinction correction, high-pass filtering, map estimation, and white noise measurements are performed. The reduction algorithm builds the map by calculating at each pixel location the flux density (hereafter brightness) and measurement uncertainty, based on the measured signal and noise properties of the relevant bolometers. Finally, spatial filtering to suppress signals on scales  $>200''$  is applied to each JCMT Transient map reconstruction to optimize the extraction of compact sources (for additional details, see Chapin et al. 2013; Mairs et al. 2017b).

The inherent 2'' to 6'' pointing uncertainty of the JCMT (Mairs et al. 2017b) is corrected by using a cross-correlation technique (see S. Mairs et al. 2022, in preparation), allowing for subarcsecond relative alignment accuracy across epochs. Each aligned map is smoothed using a 6'' (2 pixel) FWHM Gaussian kernel in order to reduce pixel noise, slightly broadening the 850  $\mu\text{m}$  FWHM beam to 15''. The relative brightness is calibrated by tracking the peak brightness of a large sample of submillimeter sources in each region over all epochs and weighting their contributions to the calibration normalization by their individually measured signal to noise (see S. Mairs et al. 2022, in preparation). The alignment and relative calibration techniques achieve better than 2% accuracy in the relative calibration at 850  $\mu\text{m}$  (Mairs et al. 2017b; S. Mairs et al. 2022, in preparation), an improvement on the nominal brightness calibration of 8% for standard reductions (Mairs et al. 2021).

### 2.3. Normalized Standard Deviation and Normalized Epoch Residuals

Our goal in this paper is to search for objects that are bright in a single epoch. To discover these flares, we first measure a standard deviation map that describes the noise at every pixel location in the field. We then compare each map of the region by its standard deviation map to identify outliers as possible transient objects.

The standard deviation of the brightness at any pixel location, calculated by considering all epochs, can be compared against the expected measurement uncertainty at that location to search for unknown variable sources. In practice, in order to properly account for the significant increase in measurement noise toward the edge of each region, we use the square root of the average of the squares of the epoch-specific uncertainty measurements at the fixed location, derived during the map-making process (see Section 2.2). With such an approach, and assuming Gaussian statistics, the mean of the normalized standard deviation map tends to unity, and the range of normalized values is inversely proportional to the root of the number of included epochs. Equivalently, the histogram of the values in the normalized standard deviation map can be approximated by a Gaussian with a peak at one and a width  $N_{\text{epochs}}^{-1/2} \sim 0.15$ , for  $N_{\text{epochs}} = 30\text{--}70$ . Thus, for the regions analyzed here a  $5\sigma$  outlier in the normalized standard deviation map should have a pixel value of 1.8, whereas a  $25\sigma$  outlier will have a pixel value close to 5.

When analyzing the normalized standard deviation maps, localized sources with significantly enhanced variability above the measurement noise will be evident by eye or can be detected by automated routines as described in Section 3.1. Care must be taken, however, when searching intrinsically bright areas within each map, as the calibration uncertainty becomes comparable in magnitude to the measurement noise for sources brighter than 500 mJy beam $^{-1}$ . Furthermore, the JCMT focus is not always sharp and thus the 850  $\mu\text{m}$  beam sidelobes can produce excess emission up to distances  $\sim 30''$  from bright peaks (for details on the properties of the JCMT beam; see Mairs et al. 2021). Given that the individual epochs are brightness calibrated using the peak brightness of known sources, this excess focus uncertainty mostly adds a positive signal to the map, leading to a noise component slightly asymmetric around zero. To account for brightness calibration and focus issues, we divide each star-forming region into two areas depending on whether the mean brightness, averaged over all epochs, lies above or below 100 mJy beam $^{-1}$  (equivalently, eight times the single epoch uncertainty of

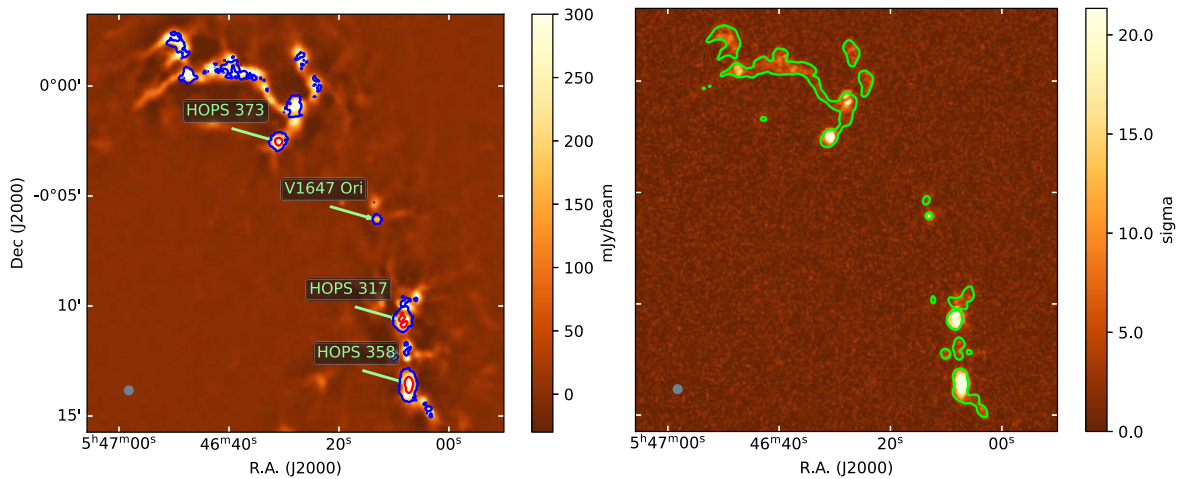


**Figure 1.** A subsection of the NGC 2068 region in Orion. Left:  $850\ \mu\text{m}$  mean brightness map, combining all 52 monitored epochs. Right: normalized standard deviation map. In the right panel, the green contour traces the location where the mean brightness reaches  $100\ \text{mJy}\ \text{beam}^{-1}$ . Note that within these zones the normalized standard deviation is often enhanced over the rest of the map. In the left panel, the blue (red) contour traces where the normalized standard deviation is greater than  $5\sigma$  ( $25\sigma$ ) above the mean. Beam-sized circular peaks in the normalized standard deviation map are evident at the locations of three known bright protostars, V1647 Ori, HOPS 358, and HOPS 373, and an arc-like feature, associated with beam shape variations is seen for HOPS 317. Additional complex features are found in the normalized standard deviation map within  $30''$  of all bright structures. The  $100\ \text{mJy}\ \text{beam}^{-1}$  contour effectively confines this enhanced measurement uncertainty.

**Table 2**  
JCMT Transient Survey Regions Statistics

Region	Faint Coverage (%)	YSOs	YSO Coverage (%)	Candidate Detections ( $\sigma$ )
IC 348	99.7	133	0.8	...
NGC 1333	98.7	80	0.5	3.3
NGC 2024	98.0	193	1.1	...
NGC 2068	98.9	97	0.6	4.4
OMC 2/3	95.9	358	2.2	25.9, 4.0, 3.7
Ophiuchus	98.5	109	0.7	...
Serpens Main	99.0	56	0.3	4.0, 3.0
Serpens South	98.4	217	1.3	...

$12\ \text{mJy}\ \text{beam}^{-1}$ ). Typically, only a few percent of the area within each region lies above this threshold (see Table 2).

Figure 1 presents the mean brightness and normalized standard deviation maps for a subsection of the NGC 2068 star-forming region in Orion. The green  $100\ \text{mJy}\ \text{beam}^{-1}$  contour marking the boundary between high and low mean brightness areas is overplotted on the normalized standard deviation map (right panel), showing that the anomalously high standard deviation measurements are almost entirely confined to these bright regions within the map. Similarly, estimated  $5\sigma$  anomalous normalized standard deviation contours are overplotted on the mean brightness map (left panel) in blue. Red contours denote regions of extreme,  $25\sigma$ , normalized standard deviation, highlighting the protostars HOPS 373 to the north and HOPS 358 to the south, as well as beam focus complications toward a bright nonvariable protostar, HOPS 317. These bright sources are best analyzed directly via their lightcurves. The multiwavelength time variability of HOPS 373 has been investigated in detail by Yoon et al. (2022), while Lee et al. (2021b) found both HOPS 373 and HOPS 358 to be robust submillimeter variables.

When searching for sources that vary in only one epoch, such as rare flaring events, the normalized standard deviation map is not exactly the most appropriate tool, because individual events themselves have a disproportionate effect on the

standard deviation. For such events it is more effective to subtract each individual epoch from the mean brightness determined using all other epochs, i.e., excluding the epoch of interest, to produce a single epoch residual brightness map. To quantify the significance of residual map peaks, we again apply a normalization by dividing the residual at each pixel by an expected measurement uncertainty. In this case there are two relevant contributions to the measurement uncertainty: (1) epoch-specific uncertainties that depend on the particulars of the observing conditions and (2) location-specific uncertainties which account for both intrinsic, ongoing source variability and anomalous measurement uncertainties due to, for example, nearby sources. We again take the epoch-specific uncertainty measure directly from the map-making process (see Section 2.2), and here we equate the location-specific measure with the standard deviation of the brightness at each pixel across all other epochs. We then normalize every single epoch residual map by the larger of these two uncertainty values. As a guide, in Table 1, the epoch-specific measurement uncertainty ranges for each region are presented. For this calculation, only those areas lying below the  $100\ \text{mJy}\ \text{beam}^{-1}$  contour and within the central  $15'$  radius of each region are utilized, ensuring that the time integration per pixel is uniform.

These analyses were performed on the full 20–40 minute integrations. Often flare lifetimes may be shorter. The  $5.5\sigma$  detection limit of  $65\ \text{mJy}\ \text{beam}^{-1}$  corresponds to the summed integration, so a flare that lasted only  $\sim 10$  minutes would need to have a peak of  $>180\ \text{mJy}\ \text{beam}^{-1}$  to be identified. Flares that last for only a minute may be missed entirely, since each region in a map is only visited  $\sim 10$  times during a single observation (Mairs et al. 2019).

Figure 1 clearly shows the importance of location-specific measurement uncertainties within each star-forming region, especially in areas of high brightness. Figure 2 presents example single epoch residual maps of IC 348, revealing the variety of possible epoch-specific measurement uncertainty categories. While the majority of epochs are similar to 2016 January 15, where the measurement noise has  $\sigma = 11\ \text{mJy}\ \text{beam}^{-1}$  and is uniformly distributed, very occasionally an epoch will have anomalous spatially correlated noise similar to 2017 February 9,

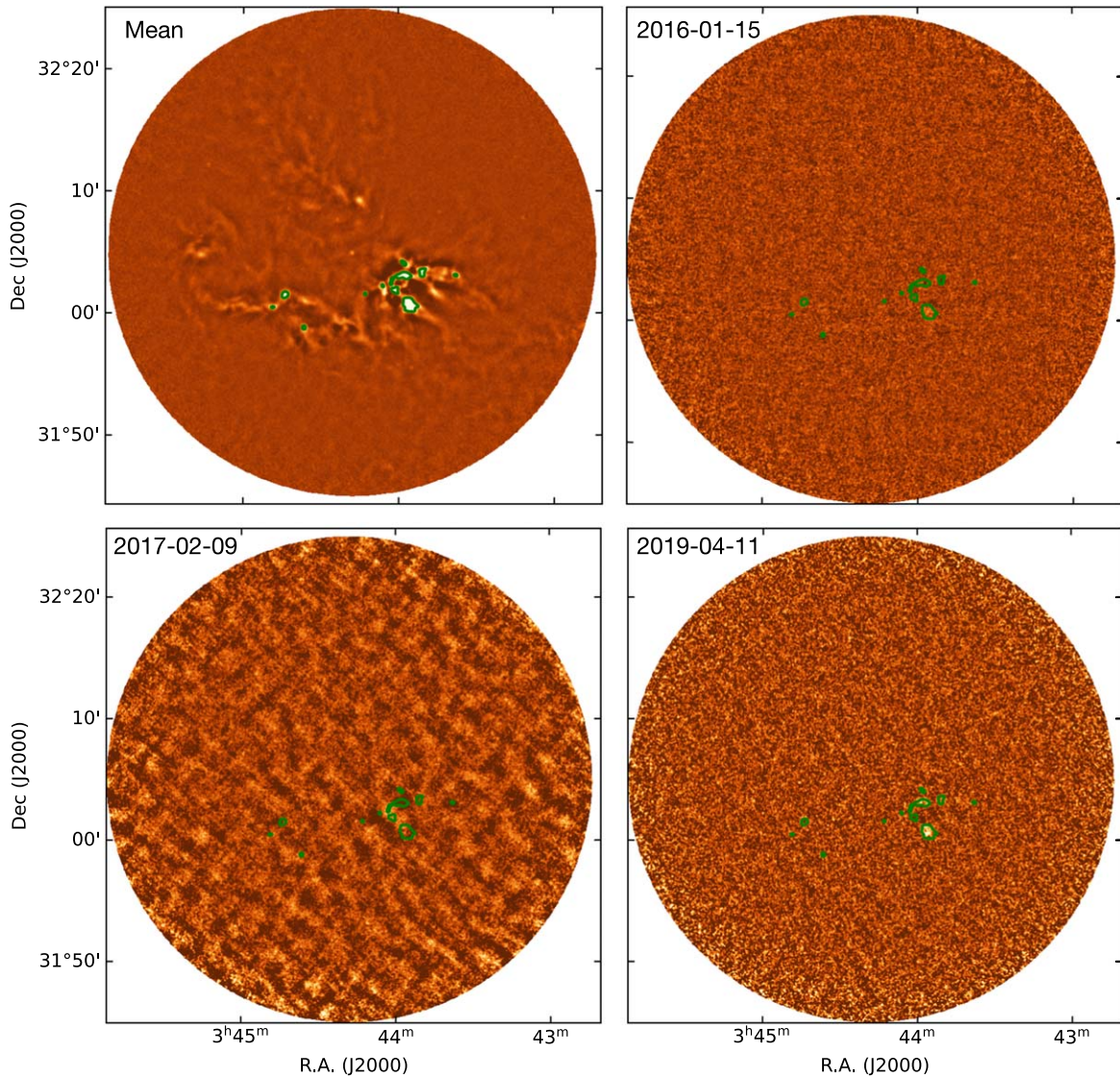


**Figure 2.** The IC 348 region in Perseus. Top left:  $850\ \mu\text{m}$  mean brightness map, combining all 34 monitored epochs ( $\sigma = 2\ \text{mJy}\ \text{bm}^{-1}$ ). Top right: a residual map for epoch 2016 January 15 ( $\sigma = 11\ \text{mJy}\ \text{bm}^{-1}$ ). Bottom left: a residual map for epoch 2017 February 9 ( $\sigma = 11\ \text{mJy}\ \text{bm}^{-1}$ ). Bottom right: a residual map for epoch 2019 April 11 ( $\sigma = 16\ \text{mJy}\ \text{bm}^{-1}$ ). All residual maps are plotted over the same range of brightness values. In each panel the green contour traces the location where the mean brightness reaches  $100\ \text{mJy}\ \text{bm}^{-1}$ . Most epochs have spatially uniform noise uncertainties similar to epoch 2016 January 15, although in poor weather the normalization may be worse, as demonstrated by epoch 2019 April 11. Rarely, more complex spatially correlated noise is found in the residual map, as shown for epoch 2017 February 9.

but where the measurement noise remains low,  $\sigma = 11\ \text{mJy}\ \text{bm}^{-1}$ . Somewhat more common are epochs, such as 2019 April 11, where the noise properties remain uniformly distributed but are enhanced due to instrument or weather conditions; in this extreme case  $\sigma = 16\ \text{mJy}\ \text{bm}^{-1}$ . Given this knowledge, after the determination of candidate single epoch variables, it is important to check for potential measurement noise anomalies in the observed epoch.

### 3. Analysis

#### 3.1. Searching for Faint Variables over All Epochs

As a first step to identifying variable sources, the normalized standard deviation maps for each region produced using all available epochs were analyzed by eye. For this analysis the  $100\ \text{mJy}\ \text{bm}^{-1}$  contour was used to mark the bright areas, with their known higher residual uncertainty, as distinct from the

bulk of each map where the noise properties are significantly more uniform. Although not the focus of this paper, within the bright areas of these star-forming regions we often find circularly shaped localized residuals at the locations of embedded protostars. In all cases, these sources were previously known to vary in brightness and are more effectively investigated via their lightcurves (Johnstone et al. 2018; Lee et al. 2021b). The confined bright areas also present arc-like residuals tracing the extended sidelobes of the telescope beam due to focus issues (see, for example, the location of HOPS 317 in the right panel of Figure 1). Alternatively, within the low brightness areas of these star-forming regions, by eye we find only two locations with significantly enhanced normalized standard deviation measurements. These locations are coincident with JW 566 in OMC 2/3 (Figure 3), previously discovered as a transient source by Mairs et al. (2019), and a Spitzer-identified candidate Class II YSO in NGC 2023, source MGM12 2864 (hereafter Source

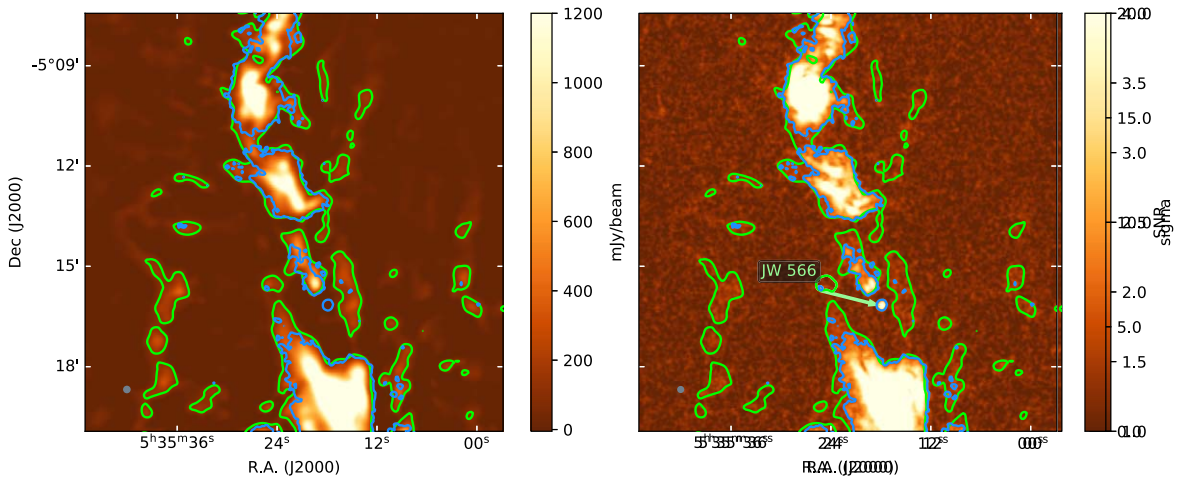


**Figure 3.** A subsection of OMC 2/3 in Orion. Left: 850  $\mu\text{m}$  mean brightness map, combining all 42 monitored epochs ( $\sigma = 2 \text{ mJy beam}^{-1}$ ). Right: normalized standard deviation map over all monitored epochs. In both panels the green contour traces the location where the mean brightness reaches  $100 \text{ mJy beam}^{-1}$  and the blue contour marks where the normalized standard deviation reaches  $5\sigma$  above the mean. JW 566 stands out clearly in the normalized standard deviation map but is too faint to be observed in the mean brightness map despite the exquisite map sensitivity.

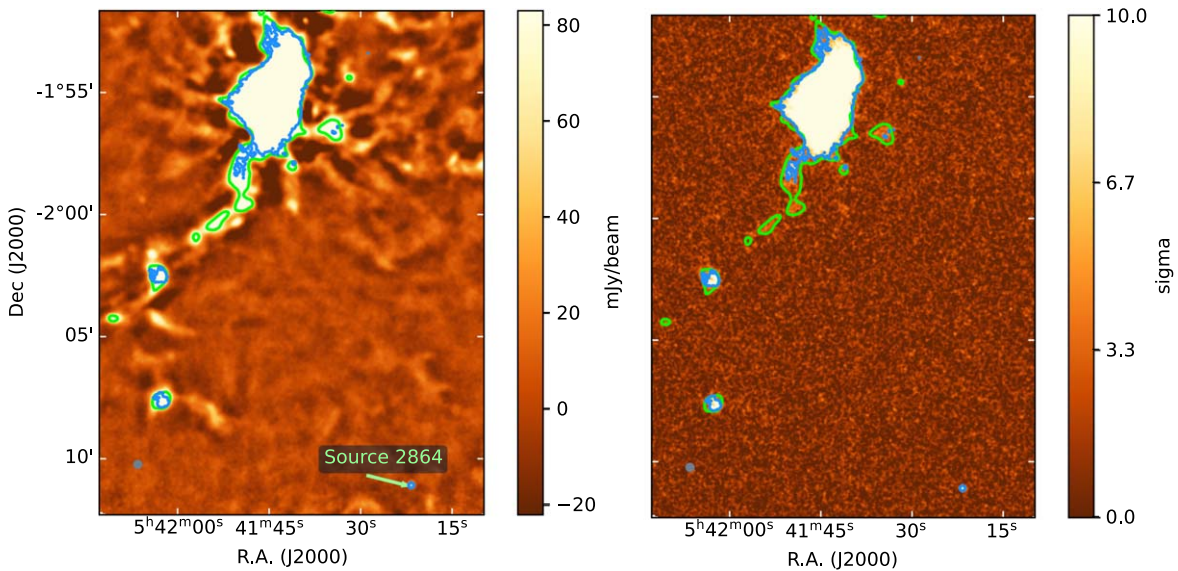


**Figure 4.** A portion of the NGC 2024 region in Orion, with NGC 2023 just off the bottom of the mapped area. Left: 850  $\mu\text{m}$  mean brightness map, combining all 43 monitored epochs ( $\sigma = 2 \text{ mJy beam}^{-1}$ ). Right: normalized standard deviation map over all monitored epochs. In both panels the green contour traces the location where the mean brightness reaches  $100 \text{ mJy beam}^{-1}$  and the blue contour marks where the normalized standard deviation reaches  $5\sigma$  above the mean. A single object, Source 2864, stands out at the bottom right of the normalized standard deviation map. While faint, this object is also observed in the mean brightness map.

2864) in the catalog by Megeath et al. (2012, MGM12), at the edge of the NGC 2024 map (Figure 4).

An automated procedure was used to search each star-forming region for evidence of anomalous standard deviation measurements at the locations of the known YSOs. For this analysis we utilized the Spitzer-based YSO catalogs by Megeath et al. (2012), Stutz et al. (2013), and Dunham et al. (2015). In Table 2 we count the YSOs within the faint brightness area of each region, where the number ranges from 56 (Serpens Main) to 358 (OMC 2/3). These YSOs occupy a small fraction, typically a few percent, of each region’s area (see Table 2). Thus, the range of normalized standard deviation measures found within each map can be used to determine the likelihood that a large value found at the location of a YSO is due to intrinsic source variability.

In detail, a roughly beam-sized box of 5 by 5 pixels ( $15''$  by  $15''$ ) was centered on each YSO location to ensure that the peak was well sampled despite a several arcsecond uncertainty in absolute image registration. The fifth-largest pixel value in the box was used as a proxy for the source variability in order to minimize the shot noise associated with individual pixels due to the pixel gridding oversampling the beam. This value was then compared against both the total number of pixels higher than that value across the rest of the normalized standard deviation map, excluding areas with bright emission, and the fractional area of the map containing YSOs to estimate the likelihood of such an enhanced YSO brightness deviation measurement within the region being due to random chance. The False Alarm Probability (FAP), therefore, decreases when the fifth-largest pixel value in a given YSO increases and as the number of known YSOs within a region decreases.

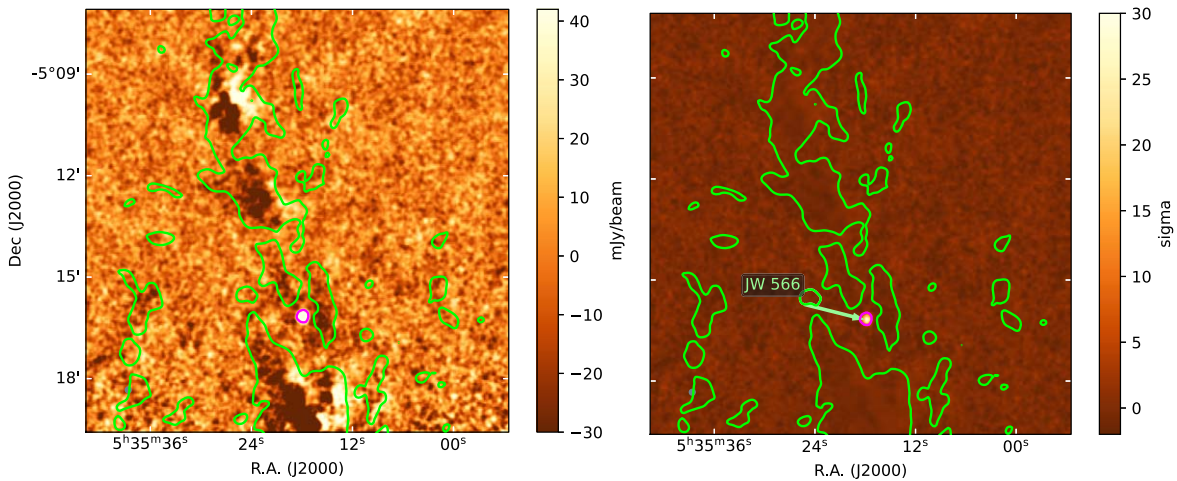


**Figure 5.** A subsection of OMC 2/3 in Orion. Left:  $850\ \mu\text{m}$  residual brightness map after subtracting the mean brightness over all other epochs from epoch 2016 November 26. Right: a normalized residual map for epoch 2016 November 26. In both panels the green contour traces the location where the mean brightness reaches  $100\ \text{mJy}\ \text{bm}^{-1}$  and the magenta contour marks where the normalized residual map reaches  $5\sigma$  above the mean. JW 566 stands out clearly in both the residual map and the normalized residual map. These images should be compared against Figure 3.

We set a relatively shallow FAP threshold of 10% for candidate faint variables within each individual region, in order to test for variables near the sensitivity limit, yielding an expectation of one potential false alarm over the eight analyzed regions. In total, seven candidates were recovered by this process. Five of the candidates were subsequently withdrawn after being found to lie extremely close to the  $100\ \text{mJy}\ \text{bm}^{-1}$  contour where the residual uncertainty could be seen to spatially spread. The only two robust detections via the automated process are the same sources as found by eye, JW 566 in OMC 2/3 (FAP  $< 0.01\%$ ) and Source 2864 in NGC 2023 (FAP  $< 3\%$ ).

### 3.2. A Blind Search for Transient Variables by Epoch

Following the approach developed in Section 3.1, for each region the individual epochs were analyzed carefully to search for transient events localized in time. Here, rather than using the normalized standard deviation map to uncover potential variables, we instead analyzed the normalized residual signal in each epoch, subtracting off the mean of all other epochs and dividing by the expected measurement uncertainty at each pixel (see Section 2.3). For this analysis we exclusively consider the areas within each region that lie below the  $100\ \text{mJy}\ \text{bm}^{-1}$  contour in order to avoid complications due to the brightness calibration and telescope focus.

Each star-forming region map consists of half a million pixels, or about twenty thousand independent beams.<sup>16</sup> Thus, a greater than  $4\sigma$  likelihood result is expected about once per epoch due to random chance alone. Given that 34-67 epochs are observed for each of the eight regions, at least one  $5\sigma$  false positive is expected to be found in the full sample, assuming Gaussian statistics. Thus, we first searched the normalized residual maps for each epoch of each region for anomalous residual peaks higher than  $5.5\sigma$ . Such events were found in four epochs, specifically IC 348 (2015 December 22, 2017 February 9), NGC 1333 (2015 December 22), and OMC 2/3 (2016 November 26). Inspection of the specific images, however, revealed that three of these maps contained correlated noise

resulting in extended blooms across the map and leaving enhanced normalized residuals (see, for example, the bottom right panel in Figure 2, IC 348 epoch 2017 February 9). Only epoch 2016 November 26 of OMC 2/3 (see Figure 5) contains a viable peak greater than  $5.5\sigma$ , at the location of JW 566 T Tauri star (as already reported by Mairs et al. 2019). Other than JW 566, to date within the JCMT Transient Survey, there are no epoch-specific brightening events above an upper limit of  $5.5\sigma$ . Given that the typical epoch uncertainty is  $12\ \text{mJy}\ \text{bm}^{-1}$  (Table 1) this is equivalent to  $\sim 65\ \text{mJy}\ \text{bm}^{-1}$  at  $850\ \mu\text{m}$ .

### 3.3. Searching for Single-epoch Transients of Known YSOs

At the locations of the known infrared YSOs in each region (Table 2) it is possible to search deeper within the normalized residual maps, using the procedure outlined in Section 3.2 whereby we compare the single epoch normalized residual measurements obtained at the location of the known sources against the distribution of measurements across the larger map. Again, we search for the fifth-largest pixel value within a 5 by 5 pixel region centered on each known YSO and compare against both the number of pixels with this value or higher in the full map and the fraction of the map covered by YSOs. We consider candidate YSO transient events detected in a given epoch when the FAP per epoch is less than 10%. Even with this low detection threshold, we find only seven candidate events within the almost 400 JCMT Transient Survey epochs. This is somewhat less than the 40 events expected solely due to the FAP threshold, suggesting that the locations of YSOs are slightly less variable than the rest of each map (potentially due to leakage of excess uncertainty across the  $100\ \text{mJy}\ \text{bm}^{-1}$  boundary). Furthermore, all of the seven candidate events have a peak residual normalized signal below  $4.5\sigma$  (see Table 2), with the exception of JW 566, which reaches  $25.9\sigma$  (Figure 5). The large increase in the significance of the JW 566 detection due to the epoch-specific analysis versus the all-epoch analysis is expected because the extraordinary brightening event is removed from the epoch-specific determination of the expected standard deviation across epochs. Similarly, the lack of detection of significant variability from Source 2864 in NGC 2023 via the epoch-specific analysis suggests that it did not undergo a single transient event, but rather it is a faint

<sup>16</sup> Recall that the map pixels are  $3''$  in length and the smoothed  $850\ \mu\text{m}$  JCMT beam has a FWHM of  $\sim 15''$ .

long-term submillimeter variable source. We discuss further the enigmatic Source 2864 in Section 4.2.

Across eight star-forming regions, the JCMT Transient Survey covers 1200 YSOs (Table 2). Furthermore, each region has about 40 epochs to date (Table 1). In total, roughly 50,000 individual YSO 850  $\mu\text{m}$  brightness measurements and single epoch normalized residuals have been made by the JCMT Transient Survey. Assuming Gaussian statistics, we therefore expect at least one  $\sim 4.5\sigma$  event just by random chance. As such, the YSO candidates identified above with peaks lower than  $4.5\sigma$  are not robust. With the exception of the extraordinary bursting event coincident with JW 566, we therefore assert that there are no epoch-specific YSO brightening events above an upper limit of  $4.5\sigma$ ,  $\sim 55 \text{ mJy bm}^{-1}$  at 850  $\mu\text{m}$  in the JCMT Transient Survey data set.

## 4. Discussion

### 4.1. Submillimeter Flaring Events from YSOs

Mairs et al. (2019) discovered an extreme flaring event from the T Tauri star JW 566 within the JCMT Transient Survey monitoring of OMC 2/3. We also recover JW 566 through our more detailed analysis of all regions and epochs to date. Our search of known, infrared-selected YSOs reveals no additional detections of single-epoch brightening events larger than  $4.5\sigma$ , i.e.,  $\sim 55 \text{ mJy bm}^{-1}$ , or equivalently a factor of 8 fainter in brightness than JW 566. Our blind analysis also reveals zero other single-epoch transient events larger than  $5.5\sigma$ , or  $65 \text{ mJy bm}^{-1}$ .

This robust nondetection is surprising given the expectation that flaring events, like most stochastic distributions, are thought to follow a power-law distribution with a greater number of events at lower brightness. For example, Getman & Feigelson (2021) find that  $dN/dL_X \propto L_X^{-\alpha}$ , with  $\alpha \sim 2.1$  for both diskless and disk-bearing pre-main-sequence stars, when  $L_X > 10^{32.5} \text{ erg s}^{-1}$ . Furthermore, the JW 566 event was observed to decay by  $\sim 50\%$  over the half-hour epoch (Mairs et al. 2019), which implies that it would have remained observable above our  $\sim 55 \text{ mJy bm}^{-1}$  threshold for at least an hour, assuming a linear decay, or two hours, if the decay were exponential. Taken together, these arguments imply that one should expect fainter detections than bright ones. We therefore conclude that the JW 566 submillimeter flaring was an exceptional rare or unique event and that its occurrence rate within the JCMT Transient Survey is not directly related to an underlying power-law distribution of bursts.

The JCMT Transient Survey has monitored about 1200 infrared-selected YSOs for about 40 epochs each, equivalently 50000 individual half-hour observations. Additional Class III (diskless) YSOs are likely present in the field, a missing and older population that is often revealed through analysis of Gaia astrometry. This represents about 1000 days, equivalently 3 yr, of 850  $\mu\text{m}$  monitoring of a random YSO. Taking our nondetection threshold at  $\sim 55 \text{ mJy bm}^{-1}$  and assuming a distance of 400 pc for the typical monitored YSO, this converts to a radio luminosity threshold of  $L_R \sim 10^{19} \text{ erg s}^{-1} \text{ Hz}^{-1}$ , above which we assert that there have been no YSO radio flaring events detected, other than the exceptional source JW 566. Assuming the Güdel & Benz (1993) scaling relation between radio and X-ray luminosity, yields a lower limit X-ray luminosity of  $L_X \sim 10^{34} \text{ erg s}^{-1}$ . This remains an extremely high threshold, on par with the brightest X-ray flares in the superflare sample by

Getman & Feigelson (2021) and likely at the limit where X-rays are saturated and cannot further increase in luminosity. The nearest star-forming region within the JCMT Transient Survey, Ophiuchus, is approximately three times closer than this nominal distance. For this region, the 100 YSOs, monitored over 34 epochs and corresponding to 70 days of observation of a single YSO, yield an upper limit on radio luminosity from flares of  $L_R \sim 10^{18} \text{ erg s}^{-1} \text{ Hz}^{-1}$  (or  $L_X \sim 10^{33} \text{ erg s}^{-1}$ ).

As discussed in Section 2.1, radio flares may vary on timescales shorter than the standard half-hour JCMT epoch integrations. Thus, care must be taken in considering the limits presented here—which assume a constant brightness throughout the observation—when comparing with models or other radio surveys. Furthermore, while each epoch integration is approximately thirty minutes, the detector array is substantially smaller than the image field of view, and thus the brightness measurement at any given location is an average over a summation of shorter, time-separated integrations (for details, see Mairs et al. 2019).

As noted in the introduction, all-sky millimeter surveys with ACT and SPT (Guns et al. 2021; Naess et al. 2021) have caught a handful of radio flares from young stars at luminosities close to the nondetection threshold presented here. Planned campaigns by the CCAT-prime collaboration (CCAT-Prime collaboration et al. 2021) and the CMB-S4 consortium (Abazajian et al. 2019) should add significantly to this sample. JW 566, however, remains almost an order of magnitude brighter than any of these other detections. For older M stars, millimeter monitoring for radio flares in the millimeter by MacGregor et al. (2018) and MacGregor et al. (2020) has uncovered small flares but no superflares. Finally, we note that the JW 566 flare is doubly remarkable due to both its extreme radio luminosity and its remarkably high radio frequency, the 650 GHz measurement being almost an order of magnitude higher in frequency than either the ACT or SPT detections (Mairs et al. 2019).

We therefore speculate that the rareness of the event may be due to a requirement that to be observed at high (submillimeter) frequencies, the event must also be extremely strong. Turning the hypothesis around, such a scenario would introduce a minimum luminosity threshold for submillimeter flares, which could explain the lack of lower brightness detections by the JCMT Transient Survey. Observational confirmation of this scenario would require the detection of additional bright flares at 650 GHz, similar to that of JW 566, while no fainter events are detected.

Interestingly, JW 566 is a known binary system (Daemgen et al. 2012) with a disk around at least one component, as seen at mid-IR and millimeter wavelengths (Megeath et al. 2012; Hacar et al. 2018). This might increase the complexity of the magnetic structure of the system and its interaction with the surrounding disk material. Indeed, radio synchrotron emission has been mapped in the hierarchical system V773 Tau A (Massi et al. 2006; Torres et al. 2012), which has four components, including a tight inner binary. The enhanced activity has been shown to be produced by interacting helmet streamers, and at periastron the radio brightness can be raised to more than 30 times that at apoastron (Adams et al. 2011). The spectroscopic binary DQ Tau also exhibits strong millimeter flares that erupt at the periastron (Salter et al. 2010). Unlike V773 Tau A or DQ Tau, JW 566 has only produced one observable powerful flare thus far, however, it remains intriguing to speculate that this single

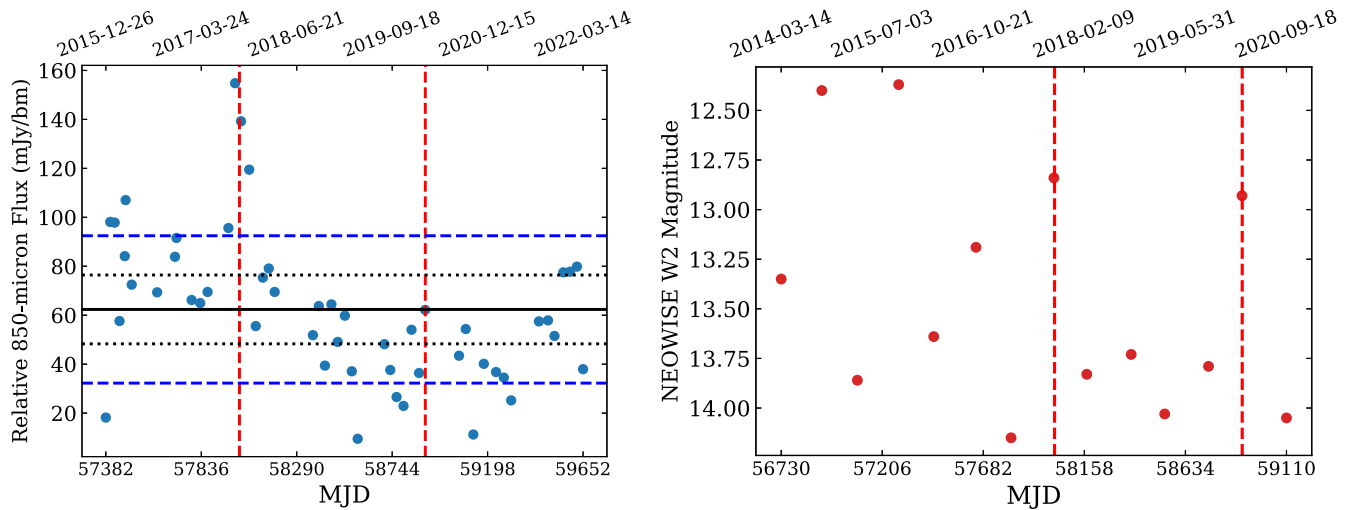


**Figure 6.** Left: JCMT submillimeter 850  $\mu\text{m}$  lightcurve of Source 2864 in NGC 2023. The solid horizontal line shows the mean flux over all epochs while the dotted horizontal lines indicate the expected uncertainty due to measurement noise. The blue dashed horizontal lines indicate the measured uncertainty around the mean. Right: NEOWISE W2 4.6  $\mu\text{m}$  lightcurve of Source 2864 in NGC 2023. In both panels the red dashed vertical lines denote two mid-IR brightening events observed by NEOWISE (see text).

event highlights JW 566 as having an unusual system architecture, perhaps with at least one component also being a tight and yet-unresolved binary. The rarity of this event may be partially explained if such bright flares occur only during the periastron passage of close binaries, which are  $\sim 3\%$  of the total population (Mazzola et al. 2020; Kounkel et al. 2021).

#### 4.2. An Enigmatic Blazar Masquerading as a YSO Candidate

Along with JW 566 in OMC2/3, our search for faint transient events uncovers a multiepoch variable near the southern edge of the NGC 2024 star-forming region field, at R.A. 05:41:21.7, decl.  $-02:11:08.3$ , associated with Source 2864 in Megeath et al. (2012) and also GBS-VLA J054121.69  $-021108.3$ . This source is likely a blazar, as indicated by a parallax consistent with a background object (Kounkel et al. 2017), but it has at times been previously classified as a Class II YSO (Megeath et al. 2012) due to its spectral energy distribution and its location within an active star-forming region and rejected as a quasar because of the YSO classification.

In contrast with JW 566, Source 2864 is detected in every epoch of submillimeter monitoring of the field. The left panel of Figure 6 reveals a dimming over time, with a short months-long burst in 2017 September–December. Over all epochs, the mean peak brightness at 850  $\mu\text{m}$  is  $S = 53 \text{ mJy bm}^{-1}$  while the variation around the mean is  $\sigma = 28 \text{ mJy bm}^{-1}$ , a factor of two larger than the calculated measurement uncertainty in the immediate vicinity of the source, 12–15  $\text{mJy bm}^{-1}$ .<sup>17</sup> This source is fainter than the brightness limits for earlier JCMT Transient analyses (Mairs et al. 2017a; Johnstone et al. 2018; Lee et al. 2021b). Nevertheless, Source 2864 has a fractional variability,  $\sigma/S \sim 0.5$ , which is similar to the strongest submillimeter variables detected in those analyses.

Source 2864 has been previously observed and classified using near through mid-IR measurements. The source is not visible in the 2MASS survey at any of J, H, or K. Based on

Spitzer mid-IR photometry, Mookerjee et al. (2009) classified it as a highly extinguished Class II source. This Spitzer classification was also assessed by Megeath et al. (2012) based on the nonextinction corrected, IRAC spectral index  $\alpha = 0.03$ . However, Povich et al. (2013) reconsidered the classification and calculated that almost 40 magnitudes of extinction are required to explain the optical through mid-IR spectral energy distribution if the source is to be considered a late-stage YSO.

The extreme extinction raises suspicions that Source 2864 is only masquerading as a YSO. It is well known (e.g., Harvey et al. 2007; Gutermuth et al. 2009; Kryukova et al. 2014) that YSOs have infrared colors similar to background galaxies and AGN (for a review, see Megeath et al. 2022). More recently, attempts to catalog galaxies using their mid-IR colors (Rakshit et al. 2019; Paggi et al. 2020) have had to deal with YSO contamination: especially for blazars and BL Lac objects. Due to its mid-IR colors, Source 2864 was included in the initial ALMA blazar catalog by Paggi et al. (2020) but subsequently culled due to its pre-existing classification as a YSO.

Indeed, many of the measured properties of Source 2864 are similar to properties of young stars in Orion. For example, Source 2864 is X-ray bright. Using ASCA, Yamauchi et al. (2000) found it to be the hardest X-ray source toward NGC 2023, with an attenuation that is converted to  $A_v \sim 30$ , similar to the extinction estimate from the infrared. The authors note that the hardness of the X-rays might also be explained with an extragalactic classification; however, the nonextinction corrected X-ray brightness is only slightly lower than for the other dozen X-ray sources revealed in the field. At the distance of Orion, the observed brightness is equivalent to  $L_x \sim 10^{30} \text{ erg s}^{-1}$ . López-García et al. (2013), using XMM-Newton, also found Source 2864 to be X-ray bright, with an uncorrected X-ray brightness similar to their other NGC 2023 targets.

While the infrared and X-ray properties are consistent with either a YSO or a background blazar, the radio properties demonstrate that the blazar interpretation is correct. Source 2864 was the brightest object in the field in a 3.6 cm survey by Reipurth et al. (2004). Kounkel et al. (2014) later noted that Source 2864 has the highest centimeter flux density reported

<sup>17</sup> As Source 2864 is near the edge of the NGC 2024 field, the surrounding measurement uncertainties are somewhat larger than the typical values of 11–12  $\text{mJy bm}^{-1}$  presented in Table 1.

for any young star. The authors also found it to be highly variable at radio wavelengths, with variations at almost the 50% level. The source remained extremely bright in follow-up VLBA observations (Kounkel et al. 2017), requiring a very small angular size for the emission region. Additionally, the VLBI image of Source 2864 reveals a core-jet structure (Petrov 2021) that is typical of extragalactic sources. More importantly, the source revealed no measurable parallax, implying a location more distant than Orion. The source is therefore almost certainly a background, extragalactic, source, which, following the mid-IR color selection by Paggi et al. (2020), we identify as a blazar.

Source 2864 is highly variable across many wavelengths—from the radio through the mid-IR (see Figure 6). Using the variability classification scheme of mid-IR NEOWISE lightcurves developed by Park et al. (2021), Source 2864 is classified as a mid-IR irregular variable with a large observed flux standard deviation. Furthermore, across the last 5.5 yr, Source 2864 is dimming in the mid-IR in a similar manner to the submillimeter. The source also undergoes occasional brightness jumps of  $\sim 1$ – $1.5$  mag, including a mid-IR burst near MJD 58000 almost coincident in time with the JCMT-observed submillimeter burst. Indeed, the three JCMT data points marking the burst span from 18 days before the NEOWISE observation to 49 days after. Unfortunately, an earlier NEOWISE burst around MJD 57250, preceded the start of the JCMT Transient Survey by 100 days and a later burst near MJD 58900 occurred just as Orion became a daytime target at the JCMT in 2020 February, unobservable for the next few months.

Similarity between observed mid-IR and submillimeter lightcurves has been previously noted for protostars by Contreras Peña et al. (2020), where the expectation is that the mid-IR traces the variable accretion rate near the protostar and the submillimeter traces the temperature response in the envelope to the accretion (see also theoretical arguments by Johnstone et al. 2013; MacFarlane et al. 2019a, 2019b; Baek et al. 2020). As anticipated theoretically, Contreras Peña et al. (2020) found that the typical fractional time-dependent response was much smaller in the submillimeter than in the mid-IR, such that  $F_{850} \propto F_{\text{mid-IR}}^{1/5.5}$ . Source 2864, however, appears to deviate significantly from this relationship, showing a factor of two brightness variations for the MJD 58000 burst in both the mid-IR and submillimeter. Furthermore, radio variability for this source has also been observed at the 50% level (Kounkel et al. 2014). We therefore speculate that multiwavelength variability can be used to classify sources, breaking the color–color diagram degeneracy between YSOs and extreme extragalactic sources.<sup>18</sup> Around YSOs, the physical environments responsible for various aspects of the spectral energy distribution, from optical through radio, are distinct and therefore can be expected to respond to system changes with differing amplitudes, and possibly time delays. For extreme extragalactic sources, such as blazars, the physical process responsible for the spectral energy distribution is less clearly understood but expected to be dominated by nonthermal processes producing a more consistent variability across wavelengths, as observed here for Source 2864. For blazars, the spectral energy distribution in the submillimeter through

mid-IR is often dominated by synchrotron emission that leads to correlated variability in this region of the spectrum (e.g., Hartman et al. 1996).

Finally, we have analyzed the JCMT submillimeter lightcurve of Source 2864 (Figure 6: left pane;) to search for potential secularly and inherent timescales.<sup>19</sup> Considering the observations prior to 2021, a robust linear fit is found with a slope of  $-12 \text{ mJy } \text{bm}^{-1}/\text{yr}$ ; however, after that date it has flattened and possibly begun to rise again. Anticipating that the lightcurve remains tied to an underlying mean brightness while undergoing significant deviations, a structure-function analysis (see Sergison et al. 2020, for methods) was performed, which found increased power on longer timescales but no clear associated intrinsic time constant. Similarly, a damped random walk analysis (see Kelly et al. 2009; Dexter et al. 2014, for methods) was performed in order to estimate a saturation timescale (the timescale beyond which the amplitude of variability does not increase), with the results suggesting a value larger than the presently monitored 5.5 yr. As shown by Bower et al. (2015), such a long submillimeter-measured saturation time is not uncommon for blazars.

## 5. Conclusions

In this paper we have analyzed 5.5 yr of JCMT Transient Survey submillimeter monitoring observations toward eight Gould Belt star-forming regions to search for evidence of variability from faint sources, primarily Class II YSOs. Eight regions, which include infrared-selected  $\sim 1200$  young stellar objects, have been monitored an average of 47 times, with each integration lasting about 30 minutes.

Here we summarize the main results of the paper:

1. When searching the normalized standard deviation maps derived using all epochs, only two robust source detections are recovered, JW 566 (Mairs et al. 2019) in OMC 2/3 (FAP  $< 0.01\%$ ) and Source 2864 (Megeath et al. 2012) in NGC 2023 (FAP  $< 3\%$ );
2. Other than JW 566, to date within the JCMT Transient Survey there are no epoch-specific brightening events above an upper limit of  $5.5\sigma$ , or  $\sim 65 \text{ mJy } \text{bm}^{-1}$  at  $850 \mu\text{m}$ . Furthermore, at the locations of known YSOs there are no epoch-specific brightening events above an upper limit of  $4.5\sigma$ ,  $\sim 55 \text{ mJy } \text{bm}^{-1}$  at  $850 \mu\text{m}$ . Taking a distance of 400 pc for the typical monitored YSO, the brightness limit above which no additional single epoch events are detected converts to a radio luminosity threshold of  $L_R \sim 10^{19} \text{ erg s}^{-1} \text{ Hz}^{-1}$ , and assuming the Güdel & Benz (1993) scaling relation between radio and X-ray, yields a threshold luminosity of  $L_X \sim 10^{34} \text{ erg s}^{-1}$ . This threshold lies at the top end of the superflare X-ray luminosity sample analyzed by Getman & Feigelson (2021). The largest radio flares, like JW 566, may access energies that are beyond the saturation limit of X-rays emission;
3. The JCMT Transient Survey has monitored about 1200 YSOs for about 40 epochs each, equivalent to 3 yr of  $850 \mu\text{m}$  monitoring of a random YSO, with only a single

<sup>18</sup> Periodic mid-IR lightcurves have similarly been used to separate background AGB stars from YSOs in the Gould Belt (Lee et al. 2021a; Park et al. 2021).

<sup>19</sup> Additional time-dependent millimeter through submillimeter observations of Source 2864 are available from ALMA, where it is used as an occasional secondary calibrator (Bonato et al. 2019). Although these data cover a range of wavelengths, they are significantly sparser than either the JCMT or NEOWISE observations and therefore not used here for time-dependent analyses.

burst event detected. The 100 YSOs in the core of Ophiuchus monitored over 34 epochs correspond to 70 days of observation of a single YSO, with no bursts detected. For the Ophiuchus sample, the upper limit on radio luminosity from flares, given our lack of detection, is  $L_R \sim 10^{18} \text{ erg s}^{-1} \text{ Hz}^{-1}$  and the assumed conversion to X-ray luminosity yields  $L_X \sim 10^{33} \text{ erg s}^{-1}$ ;

4. The powerful radio flare from JW 566 (Mairs et al. 2019), a binary T Tauri star in OMC2/3, remains a unique and rare event, perhaps related to binarity;
5. We have identified one variable quasar in approximately 1.6 sq. deg. of monitoring. The quasar, Source 2864 from Megeath et al. (2012), visually coincident with NGC 2023, is most likely a background blazar, the first extragalactic submillimeter variable source detected by the JCMT Transient Survey. Consideration of variability strength as a function of frequency across the electromagnetic spectrum may allow for better classification of sources that overlap in the mid-IR color-color diagram, such as YSOs and extreme extragalactic objects.

The authors thank the referee for the comments that improved this paper. D.J. and G.J.H. appreciate a discussion with Marina Kounkel on the VLBI parallax nondetection of Source 2864.

The authors wish to recognize and acknowledge the very significant cultural role and reverence that the summit of Maunakea has always had within the indigenous Hawaiian community. We are most fortunate to have the opportunity to conduct observations from this mountain.

The James Clerk Maxwell Telescope is operated by the East Asian Observatory on behalf of The National Astronomical Observatory of Japan; Academia Sinica Institute of Astronomy and Astrophysics; the Korea Astronomy and Space Science Institute; the Operation, Maintenance and Upgrading Fund for Astronomical Telescopes and Facility Instruments, budgeted from the Ministry of Finance (MOF) of China and administered by the Chinese Academy of Sciences (CAS), as well as the National Key R&D Program of China (No. 2017YFA0402700). Additional funding support is provided by the Science and Technology Facilities Council of the United Kingdom and participating universities in the United Kingdom and Canada. Additional funds for the construction of SCUBA-2 were provided by the Canada Foundation for Innovation. The James Clerk Maxwell Telescope has historically been operated by the Joint Astronomy Centre on behalf of the Science and Technology Facilities Council of the United Kingdom, the National Research Council (NRC) of Canada, and the Netherlands Organisation for Scientific Research. The JCMT Transient Survey project codes are M16AL001 and M20AL007.

This research used the facilities of the Canadian Astronomy Data Centre operated by NRC Canada with the support of the Canadian Space Agency. D.J. is supported by NRC Canada and by an NSERC Discovery Grant. G.J.H. is supported by a general grant 12173003 awarded by the National Science Foundation of China. H.S. is supported by the Institute of Astronomy and Astrophysics, Academia Sinica, and by grants from the Ministry of Science and Technology (MoST) in Taiwan through 109-2112-M-001-028- and 110-2112-M-001-019-.

## ORCID iDs

Doug Johnstone  <https://orcid.org/0000-0002-6773-459X>  
 Bhavana Lalchand  <https://orcid.org/0000-0003-1618-2921>  
 Steve Mairs  <https://orcid.org/0000-0002-6956-0730>  
 Hsien Shang  <https://orcid.org/0000-0001-8385-9838>  
 Wen Ping Chen  <https://orcid.org/0000-0003-0262-272X>  
 Geoffrey C. Bower  <https://orcid.org/0000-0003-4056-9982>  
 Gregory J. Herczeg  <https://orcid.org/0000-0002-7154-6065>  
 Jeong-Eun Lee  <https://orcid.org/0000-0003-3119-2087>  
 Jan Forbrich  <https://orcid.org/0000-0001-8694-4966>  
 Carlos Contreras Peña  <https://orcid.org/0000-0003-1894-1880>  
 Yong-Hee Lee  <https://orcid.org/0000-0001-6047-701X>

## References

- Abazajian, K., Addison, G., Adshead, P., et al. 2019, arXiv:1907.04473  
 Adams, F. C., Cai, M. J., Galli, D., Lizano, S., & Shu, F. H. 2011, *ApJ*, **743**, 175  
 Baek, G., MacFarlane, B. A., Lee, J.-E., et al. 2020, *ApJ*, **895**, 27  
 Benz, A. O., & Güdel, M. 2010, *ARA&A*, **48**, 241  
 Bonato, M., Liuzzo, E., Herranz, D., et al. 2019, *MNRAS*, **485**, 1188  
 Bower, G. C., Dexter, J., Markoff, S., et al. 2015, *ApJL*, **811**, L6  
 Bower, G. C., Plambeck, R. L., Bolatto, A., et al. 2003, *ApJ*, **598**, 1140  
 CCAT-Prime collaboration, Aravena, M., Austermann, J. E., et al. 2021, arXiv:2107.10364  
 Chapin, E. L., Berry, D. S., Gibb, A. G., et al. 2013, *MNRAS*, **430**, 2545  
 Cleeves, L. I., Bergin, E. A., Öberg, K. I., et al. 2017, *ApJL*, **843**, L3  
 Contreras Peña, C., Johnstone, D., Baek, G., et al. 2020, *MNRAS*, **495**, 3614  
 Currie, M. J., Berry, D. S., Jenness, T., et al. 2014, in ASP Conf. Ser. 485, Astronomical Data Analysis Software and Systems XXIII, ed. N. Manset & P. Forshay (San Francisco, CA: ASP), 391  
 Daemgen, S., Correia, S., & Petr-Gotzens, M. G. 2012, *A&A*, **540**, A46  
 Dexter, J., Kelly, B., Bower, G. C., et al. 2014, *MNRAS*, **442**, 2797  
 Dunham, M. M., Allen, L. E., Evans, N. J., II, et al. 2015, *ApJS*, **220**, 11  
 Feigelson, E. D., & Montmerle, T. 1999, *ARA&A*, **37**, 363  
 Forbrich, J., Menten, K. M., & Reid, M. J. 2008, *A&A*, **477**, 267  
 Forbrich, J., Reid, M. J., Menten, K. M., et al. 2017, *ApJ*, **844**, 109  
 Forbrich, J., Rivilla, V. M., Menten, K. M., et al. 2016, *ApJ*, **822**, 93  
 Furuya, R. S., Shinnaga, H., Nakanishi, K., Momose, M., & Saito, M. 2003, *PASJ*, **55**, L83  
 Getman, K. V., & Feigelson, E. D. 2021, *ApJ*, **916**, 32  
 Glassgold, A. E., Najita, J. R., & Igea, J. 2007, *ApJ*, **656**, 515  
 Güdel, M., & Benz, A. O. 1993, *ApJL*, **405**, L63  
 Güdel, M., Lahuis, F., Briggs, K. R., et al. 2010, *A&A*, **519**, A113  
 Guns, S., Foster, A., Daley, C., et al. 2021, *ApJ*, **916**, 98  
 Gutermuth, R. A., Megeath, S. T., Myers, P. C., et al. 2009, *ApJS*, **184**, 18  
 Hacar, A., Tafalla, M., Forbrich, J., et al. 2018, *A&A*, **610**, A77  
 Hartman, R. C., Webb, J. R., Marscher, A. P., et al. 1996, *ApJ*, **461**, 698  
 Harvey, P., Merin, B., Huard, T. L., et al. 2007, *ApJ*, **663**, 1149  
 Herczeg, G. J., Johnstone, D., Mairs, S., et al. 2017, *ApJ*, **849**, 43  
 Holland, W. S., Bintley, D., Chapin, E. L., et al. 2013, *MNRAS*, **430**, 2513  
 Johnstone, D., Hendricks, B., Herczeg, G. J., & Bruderer, S. 2013, *ApJ*, **765**, 133  
 Johnstone, D., Herczeg, G. J., Mairs, S., et al. 2018, *ApJ*, **854**, 31  
 Kelly, B. C., Bechtold, J., & Siemiginowska, A. 2009, *ApJ*, **698**, 895  
 Kounkel, M., Covey, K. R., Stassun, K. G., et al. 2021, *AJ*, **162**, 184  
 Kounkel, M., Hartmann, L., Loinard, L., et al. 2014, *ApJ*, **790**, 49  
 Kounkel, M., Hartmann, L., Loinard, L., et al. 2017, *ApJ*, **834**, 142  
 Kryukova, E., Megeath, S. T., Hora, J. L., et al. 2014, *AJ*, **148**, 11  
 Lee, J.-E., Lee, S., Lee, S., et al. 2021a, *ApJL*, **916**, L20  
 Lee, T., Shu, F. H., Shang, H., Glassgold, A. E., & Rehm, K. E. 1998, *ApJ*, **506**, 898  
 Lee, Y.-H., Johnstone, D., Lee, J.-E., et al. 2020, *ApJ*, **903**, 5  
 Lee, Y.-H., Johnstone, D., Lee, J.-E., et al. 2021b, *ApJ*, **920**, 119  
 Lin, H.-T., Chen, W.-P., Liu, J., et al. 2022, *AJ*, **163**, 164  
 López-García, M. A., López-Santiago, J., Albacete-Colombo, J. F., Pérez-González, P. G., & de Castro, E. 2013, *MNRAS*, **429**, 775  
 MacFarlane, B., Stamatellos, D., Johnstone, D., et al. 2019a, *MNRAS*, **487**, 5106  
 MacFarlane, B., Stamatellos, D., Johnstone, D., et al. 2019b, *MNRAS*, **487**, 4465

- MacGregor, A. M., Osten, R. A., & Hughes, A. M. 2020, *ApJ*, 891, 80
- MacGregor, M. A., Weinberger, A. J., Wilner, D. J., Kowalski, A. F., & Cranmer, S. R. 2018, *ApJL*, 855, L2
- Mairs, S., Dempsey, J. T., Bell, G. S., et al. 2021, *AJ*, 162, 191
- Mairs, S., Johnstone, D., Kirk, H., et al. 2017a, *ApJ*, 849, 107
- Mairs, S., Lalchand, B., Bower, G. C., et al. 2019, *ApJ*, 871, 72
- Mairs, S., Lane, J., Johnstone, D., et al. 2017b, *ApJ*, 843, 55
- Massi, M., Forbrich, J., Menten, K. M., et al. 2006, *A&A*, 453, 959
- Mazzola, C. N., Badenes, C., Moe, M., et al. 2020, *MNRAS*, 499, 1607
- Megeath, S. T., Gutermuth, R., Muzerolle, J., et al. 2012, *AJ*, 144, 192
- Megeath, S. T., Gutermuth, R. A., & Kounkel, M. A. 2022, *PASP*, 134, 042001
- Mookerjee, B., Sandell, G., Jarrett, T. H., & McMullin, J. P. 2009, *A&A*, 507, 1485
- Naess, S., Battaglia, N., Richard Bond, J., et al. 2021, *ApJ*, 915, 14
- Paggi, A., Bonato, M., Raiteri, C. M., et al. 2020, *A&A*, 641, A62
- Park, W., Lee, J.-E., Contreras Peña, C., et al. 2021, *ApJ*, 920, 132
- Petrov, L. 2021, *AJ*, 161, 14
- Povich, M. S., Kuhn, M. A., Getman, K. V., et al. 2013, *ApJS*, 209, 31
- Rakshit, S., Johnson, A., Stalin, C. S., Gandhi, P., & Hoenig, S. 2019, *MNRAS*, 483, 2362
- Reipurth, B., Rodríguez, L. F., Anglada, G., & Bally, J. 2004, *AJ*, 127, 1736
- Salter, D. M., Kóspál, Á., Getman, K. V., et al. 2010, *A&A*, 521, A32
- Salter, D. M., Hogerheijde, M. R., & Blake, G. A. 2008, *A&A*, 492, L21
- Sergison, D. J., Naylor, T., Littlefair, S. P., Bell, C. P. M., & Williams, C. D. H. 2020, *MNRAS*, 491, 5035
- Shu, F. H., Shang, H., Glassgold, A. E., & Lee, T. 1997, *Sci*, 277, 1475
- Sossi, P. A., Moynier, F., Chaussidon, M., et al. 2017, *NatAs*, 1, 0055
- Stutz, A. M., Tobin, J. J., Stanke, T., et al. 2013, *ApJ*, 767, 36
- Torres, R. M., Loinard, L., Mioduszewski, A. J., et al. 2012, *ApJ*, 747, 18
- Ward-Thompson, D., Di Francesco, J., Hatchell, J., et al. 2007, *PASP*, 119, 855
- Waterfall, C. O. G., Browning, P. K., Fuller, G. A., & Gordovskyy, M. 2019, *MNRAS*, 483, 917
- Yamauchi, S., Kamimura, R., & Koyama, K. 2000, *PASJ*, 52, 1087
- Yoo, H., Lee, J.-E., Mairs, S., et al. 2017, *ApJ*, 849, 69
- Yoon, S.-Y., Herczeg, G. J., Lee, J.-E., et al. 2022, *ApJ*, 929, 60